Draft version May 3, 2019
Typeset using LaTeX **twocolumn** style in AASTeX62

Improving Damped Random Walk parameters for SDSS Stripe82 Quasars with Pan-STARRS1.

Krzysztof L. Suberlak,[1] Željko Ivezić,[1] and Chelsea MacLeod[2]

[1] *Department of Astronomy*
University of Washington
Seattle, WA 98195, USA
[2] *Harvard Smithsonian Center for Astrophysics*
60 Garden St, Cambridge, MA 02138, USA

(Received January 1, 2019; Revised January 17, 2019; Accepted February 1, 2019)

Submitted to ApJ

ABSTRACT

We use the Panoramic Survey Telescope and Rapid Response System 1 Survey (Pan-STARRS1 or PS1) data to extend the Sloan Digital Sky Survey (SDSS) Stripe 82 quasar light curves. Combined datasets afford 15 year baselines for 9248 quasars, improving on previous studies using SDSS only. We make predictions on fidelity of DRW retrieval once ZTF and LSST data become available. We fit the light curves with Damped Random Walk (DRW) model, and correlate the DRW parameters - asymptotic variability amplitude SF_∞, and characteristic timescale τ, with quasar properties - black hole mass, bolometric luminosity, and redshift. We find that characteristic timescale τ is more strongly dependent on luminosity, and has a weaker dependence on black hole mass. The variability amplitude is less strongly dependent on the quasar luminosity.

1. INTRODUCTION

Quasars are inherently variable sources at the rms level of 0.2 mag. They are distant active galactic nuclei, harboring a supermassive black hole surrounded by a hot accretion disk. Although it is agreed upon that majority of optical emission stems from the accretion disk, the detailed origin of variability has been debated over the past 50 years (Sun et al. 2018 and references therein). Some favor a thermal origin of variability (Kelly et al. 2013), related to the propagation of inhomogeneities ("hot spots") in the disk (Dexter & Agol 2011; Cai et al. 2016), others suggested magnetically elevated disks (Dexter & Begelman 2019), or X-ray reprocessing (Kubota & Done 2018). Quasar light curves have been successfully described using the Damped Random Walk (DRW) model (Kelly et al. 2009; MacLeod et al. 2010; Kozłowski et al. 2010; Zu et al. 2011; Kasliwal et al. 2015), and the DRW parameters have been linked to the physical quasar properties. MacLeod et al. (2010) (M10) found correlations of the characteristic timescale and variability amplitude to the black hole mass, and quasar luminosity.

Variability is also a classification tool, allowing to distinguish quasars from other variable sources that do not exhibit such stochastic variability pattern (MacLeod et al. 2011). Using the DRW parametrization, (MacLeod et al. 2011) found that DRW timescale and amplitude for QSO are order of magnitude different from stars. This is especially useful for selecting quasars in the intermediate redshift range (which overlaps the stellar locus in color-color diagrams - see Sesar et al. 2007; Yang et al. 2017). Variability has also been used to increase the completeness in measurements of Quasar Luminosity Function (see Ross et al. 2013; Palanque-Delabrouille et al. 2013; AlSayyad 2016; McGreer et al. 2013, 2018).

Due to its stochastic nature, the DRW process requires the light curve to be many times longer than the characteristic timescale for an unbiased parameter retrieval. The rule of thumb is that the light curve must be at least ten times longer than its characteristic timescale (Kozłowski et al. 2010; Kozłowski, Szymon 2017). For this reason some studies have restricted the probed redshift range, limiting the quasar sample to where one would expect only shorter timescales based on previous studies (Sun et al. 2018; Guo et al. 2017). Others have

Corresponding author: Krzysztof Suberlak
suberlak@uw.edu

suffered from short-baseline biases by employing single-survey data (Hernitschek et al. 2016). Thus by extending available quasar light curves we are able to better recover a wider range of DRW timescales, and probe a wider range of redshifts and black hole masses.

Almost a decade ago MacLeod et al. (2010) (hereafter M10) published their research using the SDSS Stripe 82 data, and new datasets (PS1,PTF,CRTS) have become available since that can extend the quasar light curves by almost 50% . Indeed, (Li et al. 2018) combined SDSS and Dark Energy Camera Legacy Survey (DECaLS) data, to provide a 15 year baseline, but by focusing on a large area to encompass as many quasars as possible (119,305 up to z=4.89) suffered from poor sampling which lends itself better to an ensemble structure function approach rather than direct light curve modeling. On the other hand, (Sánchez-Sáez et al. 2018) who employed optical data from QUEST-La Silla AGN variability survey, also used the Structure Function parametrization (amplitude of variability and the excess variance), because the light curve length (less than 5 years for 2435 quasars) excluded the possibility of unbiased retrieval of characteristic timescale.

This paper improves on the DRW parameters (Section 2) describing amplitude and characteristic timescale of Stripe82 quasars by extending the SDSS light curves for well-sampled Stripe82 with PanStarrs1 (PS1) data (Sections 3 and 4). We revisit trends between the DRW parameters and physical quasar properties, such as black hole mass, or bolometric luminosity (Section 5). We make predictions for fidelity of DRW parameter retrieval once ZTF and LSST data become available. In this work we adopt a ΛCDM cosmology with $h_0 = 0.7$ and $\Omega_m = 0.3$.

2. METHODS

2.1. *DRW as a Gaussian Process*

Damped Random Walk (OrnsteinUhlenbeck process) can be modeled as a member of a class of Gaussian Processes (GP). Each GP is described by a mean and a kernel - a covariance function that contains a measure of correlation between two points x_n, x_m, separted by Δt_{nm} (autocorrelation). For the DRW process, the covariance between observations of a source separated by Δt_{nm} is :

$$k(\Delta t_{nm}) = a \exp(-\Delta t_{tm}/\tau) \quad (1)$$
$$= \sigma^2 \exp(-\Delta t_{tm}/\tau) \quad (2)$$
$$= \sigma^2 ACF(\Delta t_{tm}) \quad (3)$$

Here a or σ^2 is an amplitude of correlation decay as a function of t_{tm}, while τ is the characteristic timescale over which correlation drops by $1/e$. For a DRW, the correlation function $k(\Delta t_{nm})$ is also related to the autocorrelation function ACF.

Not explicitly used in this paper, but of direct relevance to DRW modeling, is the structure function (SF). SF can be found from the data $\{m_i, t_i\}$ as the root-mean-squared of magnitude differences Δm calculated as a function of temporal separation Δt. SF is directly related to a DRW kernel $k(\Delta t_{nm})$:

$$SF(\Delta t) = SF_\infty (1 - \exp(-|\Delta t|/\tau))^{1/2} \quad (4)$$

For quasars the SF follows approximately a power law: $SF \propto \Delta t^\beta$, and it levels out for large time lags Δt to a constant value of SF_∞. Note that $SF_\infty = \sqrt{2}\sigma$ in the above (also see MacLeod et al. (2012); Bauer et al. (2009); Graham et al. (2015) for an overview).

The likelihood is evaluated with celerite(Foreman-Mackey et al. 2017) - a fast GP solver that scales linearly with the number of data points $\mathcal{O}(N)$ thanks to an optimization that exploits the structure of covariance matrix for kernels that are a mixture of exponentials, such as a DRW kernel(Foreman-Mackey et al. 2018; Ambikasaran et al. 2015). The method employed is similar to that used by Rybicki & Press (1992); Kozłowski et al. (2010), M10 - like in previous work, we use a uniform prior on σ and τ. The main difference is that rather than adopting the Maximum A-Posteriori (MAP) as the 'best-fit' value for the DRW parameters, we find the expectation value of the marginalized log posterior. If the posterior space was a 2D Gaussian in σ, τ space, the expectation value would coincide with the maximum of the log posterior. However, due to non-Gaussian shape of the log posterior, the expectation value is a better estimate of σ and τ rather than MAP.

2.2. *The impact of light curve baseline*

K17 reports that one cannot trust any results of DRW fitting unless the light curve length is at least ten times longer than the characteristic timescale. We confirm these generic trends by repeating his simulation setup. We model 10 000 DRW light curves with fixed length (baseline) $t_{exp} = 8$ years, $SF_\infty = 0.2$ mag, SDSS or OGLE-like cadence, sampling over a range of input timescales. Given fixed baseline, this means exploring the parameter space of $\rho = \tau/t_{exp}$, $\rho \in \{0.01 : 15\}$. We simulate 100 light curves at each ρ.

To simulate observational conditions we add to the true underlying signal $s(t)$ a noise offset, $n(t)$. Like K17, we assume $n(t)$ to be drawn from a Gaussian distribution $\mathcal{N}(0, \sigma(t))$ with a width $\sigma(t)$, corresponding to the photometric uncertainty at the given epoch, $e(t)$) :

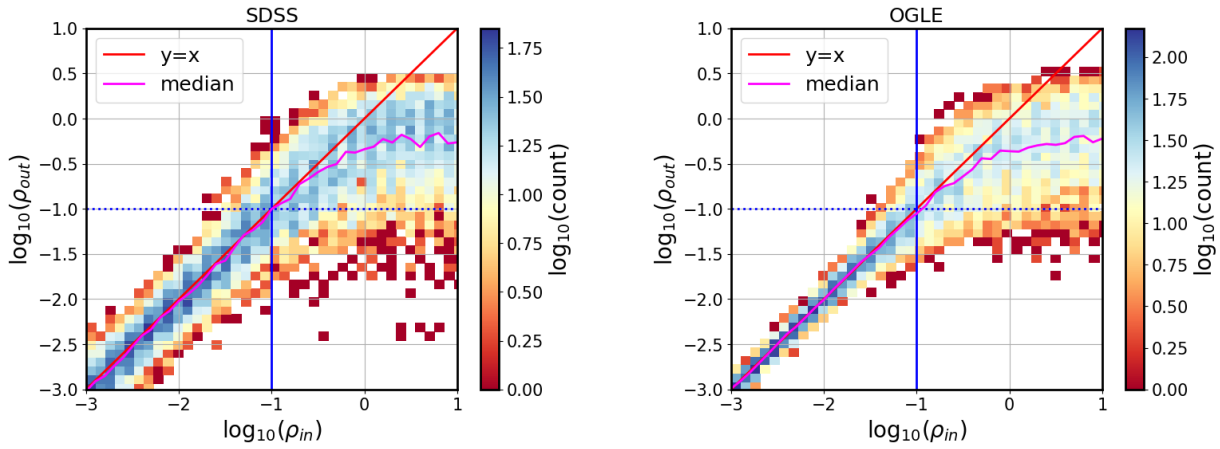

Figure 1. Probing the parameter space of $\rho = \tau/t_{exp}$, with a simulation of 10 000 light curves : 100 light curves per each of 100 ρ values spaced uniformly in logarithmic space between $\rho \in \{0.01 : 15\}$. Thus with the baseline t_{exp} set to 8 years, we sample a range of 100 input timescales, as in K17. Left panel shows the SDSS-like cadence with N=60 points, and the right panel OGLE-like cadence with N=445 points. The dotted horizontal and solid vertical lines represent $\rho = 0.1$, i.e. the baseline is ten times longer than considered timescale. The diagonal line is $y = x$, i.e. the line that would be followed if the recovered ρ (τ) was exactly the same as the input ρ (τ).

$$y(t) = s(t) + n(t) \tag{5}$$

The $s(t)$ is found by iterating over the array of time steps t. At each step, we draw a point from a Gaussian distribution, for which the mean and standard deviation are re-calculated at each timestep. Starting at t_0, the signal is equal to the mean magnitude, $s_0 = m$. After a timestep $\Delta t_i = t_{i+1} - t_i$, the signal s_{i+1} is drawn from $\mathcal{N}(loc, stdev)$, with :

$$loc = s_i e^{-r} + m\left(1 - e^{-r}\right) \tag{6}$$

and

$$stdev^2 = 0.5\,\mathrm{SF}_\infty^2\left(1 - e^{-2r}\right) \tag{7}$$

where $r = \Delta t_i/\tau$, τ is the damping timescale, SF_∞ is the variability amplitude , and m the mean magnitude. This follows the formalizm in Kelly et al. (2009) (eqs. A4 and A5) as well as in MacLeod et al. (2010) (Sec. 2.2), and is equivalent to the setup of K17.

We adopt SDSS S82-like cadence with N=60 epochs, or OGLE-III like cadence with N=445 epochs. The errors are set by the adopted mean magnitudes, $r = 17$ and $I = 18$:

$$\sigma^2_{SDSS} = 0.013^2 + \exp\left(2(r - 23.36)\right) \tag{8}$$
$$\sigma^2_{OGLE} = 0.004^2 + \exp\left(1.63(I - 22.55)\right) \tag{9}$$

Fig. 1 confirms the findings of K17: recovered ρ becomes meaningless ('unconstrained') if the available DRW light curve baseline is not at least ten times longer than the input timescale. It also means that by extending the baseline we can move from the biased region to the unbiased regime. Encouraged by this result, we extend the baselines of quasar light curves, and revisit relations studied by M10.

2.3. *Departure from DRW?*

The power spectral density (PSD) of the DRW process is:

$$P(f) = \frac{4\sigma^2\tau}{1 + (2\pi\tau f)^2} \tag{10}$$

(with $\sigma = \mathrm{SF}_\infty/\sqrt{2}$, τ is the characteristic timescale, f is the frequency), so that $P(f) \propto f^{-2}$ at high frequencies $f > (2\pi\tau)^{-1}$, and levels to a constant value at lower frequencies(Kelly et al. 2014). This can be parametrized as $P(f) \propto f^{\alpha_h}$ at high frequencies (short timescales), and $P(f) \propto f^{\alpha_l}$ at low frequencies (long timescales), so that for a pure DRW process $\alpha_h = -2$ and $\alpha_l = 0$.

Various opinions exist about the exact value of α_l and αh for accurate description of quasar variability, or more broadly speaking - AGN variability.

One approach comes from studying optical light curves of wide-field, ground-based photometric surveys, such as OGLE, SDSS, or PS1. In general, these studies used light curves with rather sparse non-uniform sampling, cadence of few epochs per week, and overall length (baseline) of the order of several years. For instance, (Zu et al. 2013) using 223 I-band OGLE quasar light curves (baseline of $\approx$ 7 years, $\approx$ 570 epochs) considered whether different covariance functions (powered-exponential, Matèrn, Kepler-exponential, Pareto exponential - see Eqs.5,6,8,9 in Zu et al. 2013) may present a

better fit, and found that while there may be small deviations, they are not significant enough to depart from a robust DRW description. Similarly, (Sun et al. 2018) found that the data quality of SDSS-like light curves is insufficient to distinguish between CAR(1) and more complex models. On the longer timescales, Guo et al. (2017) with a low-redshift subset of SDSS S82 quasars claims that the low-frequency slope α_l should not be steeper than -1.3. For the same SDSS S82 quasars, (Kozłowski, Szymon 2017) (as well as Kozłowski (2016) and (Caplar et al. 2017)) found PSD slopes $\alpha_h \leqslant -2$, which meant that models assuming a DRW $\alpha_h = 2$ would result in decorrelation timescales biased low. He stated that it is currently not possible to distinguish between close-to-DRW and DRW processes for the S82 quasars because good sampling at both low frequencies (long timescales, white noise part), and high frequencies (short timescales, red / pink noise part). However, Simm et al. (2016) used a limited PS1 sample of 90 X-ray selected AGN, and with PS1 data found that their data can be described by a broken power law with low-frequency slope of -1 and high frequency slope from -2 to -4, with a break at timescale between 200 to 300 days.

A second approach of excellent cadence but short baselines is afforded by a space based Kepler missionBorucki et al. (2010), observing without the interruption of the atmosphere. Using Kepler light curves with a half-hour cadence enabled an unprecedented view of the high-frequency part of the AGN spectrum, but the results are inconclusive. Mushotzky et al. (2011) analyzed the four AGN light curves from 2010-2011 (three separate quarters), and found evidence of steeper slopes (α_h -2.6 to -3.1). Later, Edelson et al. (2014) combined 3.4 yr worth of data (13 quarters) for an AGN Zw 229-15, and found the slope increasing from -2 to -4 at frequency corresponding to 5 day timescale. Smith et al. (2018) used 4 years of Kepler data for 21 AGN, and found slopes generally steeper than the DRW, between -2 and -3.4 . They also concluded that, in accordance with Caplar et al. (2017), perhaps AGN are described by a combination of DRW behavior, and a changing PSD, tied to an accretion duty cycle. With the original Kepler mission ending in 2013 with the failure of the second reaction wheel, it transitioned to K2, pointing at various fields around the ecliptic, which limits further the available baseline for AGN study. (Aranzana et al. 2018) conducted the most extensive study of K2 AGN light curves to date, including 252 well-sampled AGN. Using data spanning 80 days they find a range of high-frequency slopes from -1 to -3.2, with the median of -2.2, consistent with the DRW model.

The exact shape of quasar PSD would affect other areas of study. One example is reverberation mapping (RM), which was used to provide accurate black hole mass estimates. RM is based on measuring the lags between light curves observed at different wavelengths. The two most widely used approaches to measuring interband lags are interpolated cross-correlation function (ICCF, Gaskell & Peterson 1987; Peterson et al. 2004) and light curve modeling via Markov chain Monte Carlo approach (JAVELIN, Zu et al. 2011). The PSD of the DRW comes explicitly in the latter, which assumes that the higher energies drive lower energies (whether due to x-ray reprocessing or other mechanism), and that the driving light curve is well-modeled by a DRW (with PSD equal to -2 or flatter). In this scenario other light curves (at longer wavelength) are related to it via transfer function Edelson et al. (2019). Using a wrong PSD means at best that errors are underestimated. Therefore a convincing detection of a departure of quasar PSD from that of the DRW would have a direct impact on RM studies that use JAVELIN or other light curve modeling tools.

In the end, we follow the direction laid out in M10, Sec.4.4, which shows that while within S82 sampling assuming $\alpha_h = 2$ it is impossible to reliably distinguish between a $\alpha_l = 0$ and -1. A future study with appropriate cadence would be necessary to model each quasar individually with different α_l and α_h. We elect to use the DRW description ($\alpha_l = 0$, $\alpha_h = -2$) to allow a better comparison of our results with M10.

3. DATA

3.1. *Surveys*

We focus on THE data pertaining to a 290 deg^2 region of southern sky, repeatedly observed by SDSS between 1998 and 2008. Originally aimed at supernova discovery, objects in this area, known as Stripe82 (S82), were re-observed on average 60 times (see MacLeod et al. 2012 Sec. 2.2 for overview, and Annis et al. 2014 for details) . Availability of well-calibrated (Ivezić et al. 2007), long-baseline light curves spurred variability research (see Sesar et al. 2007). The catalog prepared by (Schneider et al. 2008) as part of DR9 contains 9258 spectroscopically confirmed quasars.

We extend the SDSS light curves with PanSTARRS (PS1) (Chambers 2011; Flewelling 2018), CRTS (Drake et al. 2009), and PTF (Rau et al. 2009) data. We find 9248 PS1 matches, 6455 PTF matches, and 7737 CRTS matches to SDSS S82 quasars. There are 6444 quasars with SDSS-PS1-PTF-CRTS data. Fig 2 depicts the baseline coverage of various surveys. Each survey uses a unique set of bandpasses and cadences : SDSS light curves contain near-simultaneous $\{u, g, r, i, z\}_{SDSS}$

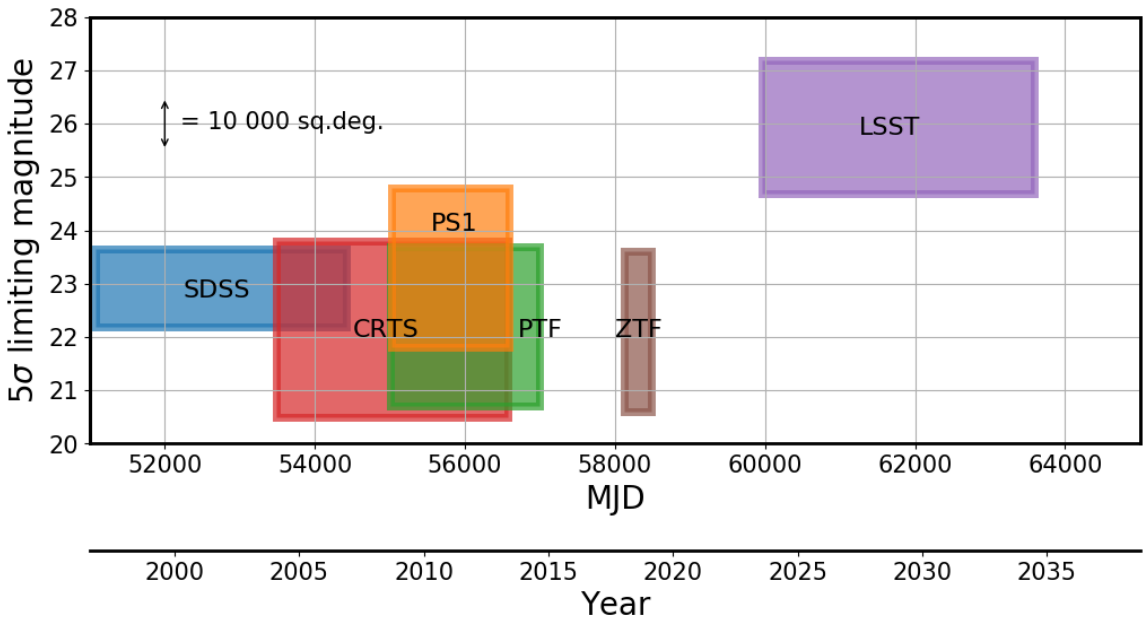

Figure 2. An illustration of survey baseline, sky area covered, and depth. The width of each rectangle corresponds to the extent of light curves available (or simulated) for Stripe 82 quasars for each survey. For SDSS this means DR7; for CRTS DR2, PS1 DR2, PTF DR2, ZTF year 2018, and LSST the full 10-year survey. The lower edge of each rectangle corresponds to the 5σ limiting magnitude (SDSS r, PS1 r, PTF R, ZTF r, LSST r, CRTS V). The vertical extent corresponds to the total survey area (for SDSS, up to and including DR15). Note how PS1 and PTF extend the baseline of SDSS by approximately 50%, and how inclusion of LSST triples the SDSS baseline. For reference, the area covered by LSST is 25000 sq.deg., which corresponds to 60% of the sky. The whole sky has an area of 4π steradians (41253 sq.deg.).

, and the others are non-simultaneous : $\{g,r,i,z,y\}_{PS1}$, $\{g,R\}_{PTF}$, V_{CRTS}.

3.2. *Photometric offsets*

We combine the photometry into a single 'master' bandpass. We choose SDSS r as the target since it has the best photometry, and we calculate color terms that afford transformation from other photometric systems to SDSS. We elect only to translate to SDSS r photometry from nearby filters : ($\{g,R\}_{PTF}$, $\{g,r,i\}_{PS1}$, V_{CRTS}).

Color terms are derived using SDSS standard stars catalog (Ivezić et al. 2007). We focused on 10% subset of randomly chosen stars from the catalog, and found CRTS (B.Sesar, priv.comm.), PS1 (from MAST http://panstarrs.stsci.edu) and PTF (IRSA PTF Object Catalog https://irsa.ipac.caltech.edu/) matches.

We consider the difference between the target (SDSS) and source (eg.PS1) photometry as a function of mean SDSS $(g-i)$ color :

$$m_{PS1} - m_{SDSS} = f(g-i) \tag{11}$$

While Tonry et al. (2012) chose to spread the stellar locus with $(g-r)$ color, we prefer to use the $(g-i)$ color since it provides a larger wavelength baseline. Some authors (eg. Li et al. (2018)) allow $f(g-i)$ to be a higher-order polynomial, but since we limit the transformation to the region of $(g-i)$ space occupied by quasars (Fig. 3), we find that the linear fit is sufficient (see Fig. 4). Table 1 shows the offsets used to transform PS1, CRTS and PTF to SDSS r-band.

4. SIMULATIONS : LESSONS LEARNED

We simulate the theoretical improvement in the retrieved DRW parameters in combined light curves by generating long and well-sampled light curves, all with input $\tau = 575$ days, $SF_\infty = 0.2$ mag (the median of S82 distribution in M10). We then select SDSS, or SDSS-PS1 segments, sampling at the cadence corresponding to real light curves. We also predict the contribution of ZTF and LSST data (Fig. 5). For the ZTF 1-year segment (Spring 2019 ZTF Data Release will include data from 2018) we assumed 120 observations in ZTFg and ZTFr (every three nights), deriving the error model from the ZTF data for standard stars (Fig. 6). For the LSST 10-year segment (final LSST DR10 in 2031) we assumed 50 epochs per year, randomly distributed throughout the year, with the following error model:

$$\sigma_{LSST}(m)^2 = \sigma_{sys}^2 + \sigma_{rand}^2 \ (\mathrm{mag})^2 \tag{12}$$

$$\sigma_{rand}^2 = (0.04-\gamma)x + \gamma x^2 \tag{13}$$

$$x = 10^{0.4(m-m_5)} \tag{14}$$

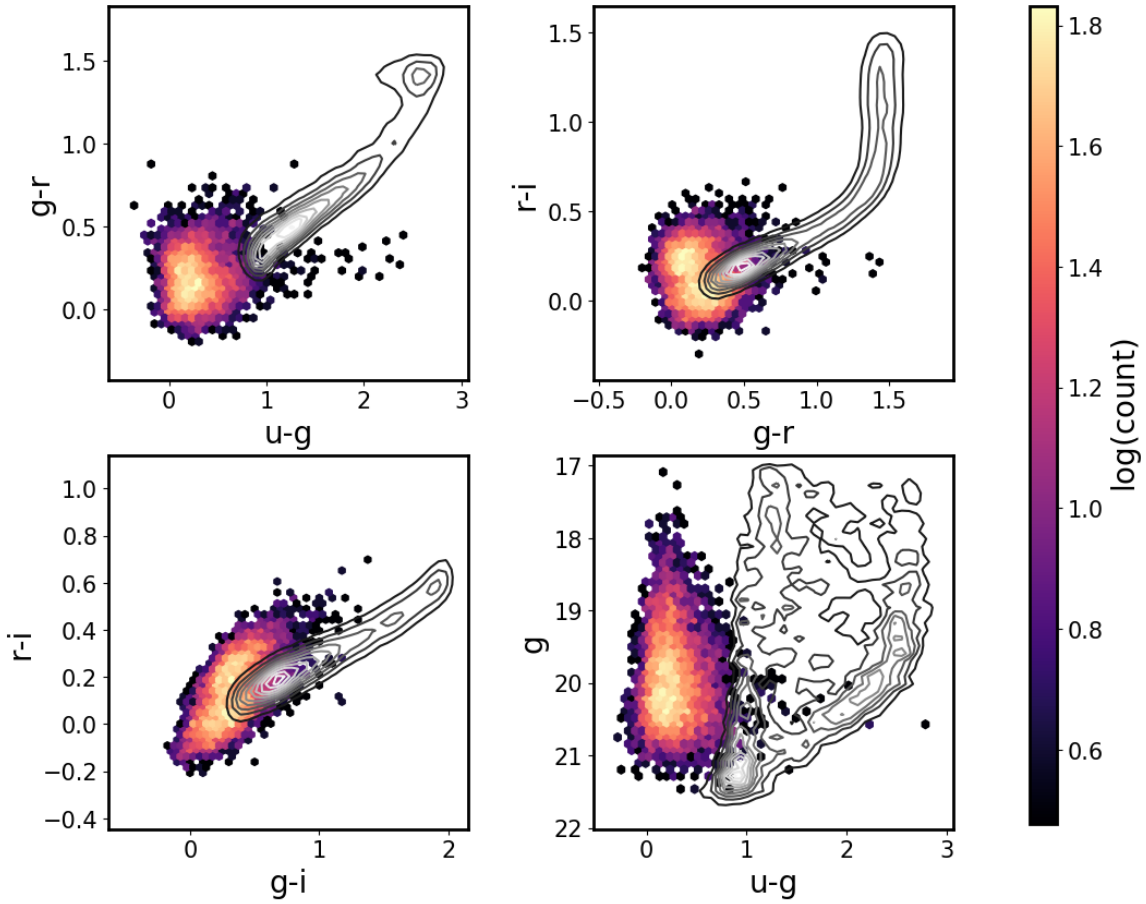

Figure 3. Regions occupied in color-color space by S82 quasars (colors) and standard stars (contours) (Schneider et al. 2010). We show only 10 000 randomly chosen stars from the full 1 mln + standard stars catalog Ivezić et al. 2007. We limit the offset to SDSS $-0.5 < (g-i) < 1.$. Quasars also overlap other variable sources (eg. RRLyrae), not shown on this illustration Sesar et al. 2007.

with $\sigma_{sys} = 0.005$, $\gamma = 0.039$, $m_5 = 24.7$ (see Sec. 3.2 in Ivezić et al. (2019)).

To mirror observational conditions we add to the true underlying DRW signal a Gaussian noise, with variance defined by photometric uncertainties for corresponding surveys. Given the noise properties of each survey (Fig. 7), we found that relatively large uncertainties of CRTS and PTF segments introduced less improvement in recovery of DRW parameters, given that similar baseline is already covered by the PS1 data. We further found that inclusion of ZTF data for 2018 would not significantly change our results. Inclusion of PS1 data with its excellent photometry (as compared to ZTF or PTF) is the best improvement over existing SDSS results. In the future (after more data has been assembled and recalibrated) ZTF will help, but not as dramatically as LSST (see Fig. 8). For this reason we found that using only SDSS-PS1 portion is the best tradeoff between adding more baseline vs introducing more uncertainty with noisy data. Fig. 5 illustrates of the simulated light curve.

As we found earlier, extending the light curve baseline decreases the bias in the retrieved DRW parameters (Fig. 1). For light curves that simulate the extension of SDSS with PS1, ZTF, LSST segments, Figs. 8 and 9 show that this is indeed the case: as make light curves longer, the retrieved τ and SF_∞ become more centered on the input value.

5. RESULTS: FITTING SDSS-PS1 WITH CELERITE

We have extended the baseline of Stripe82 quasars by adding to SDSS r-band data the PS1 g,r,i data, transformed into common SDSS r-band. As the variability originates in the accretion disk, we shift all timescales to quasar rest frame : $\tau_{\rm RF} = \tau_{\rm OBS}/(1+z)$.

We first show that our results are consistent with M10 when using only the SDSS r-band : on Fig. 10) the distributions of τ, SF_∞ from M10 (red) and our results (blue) coincide. Furthermore, when comparing

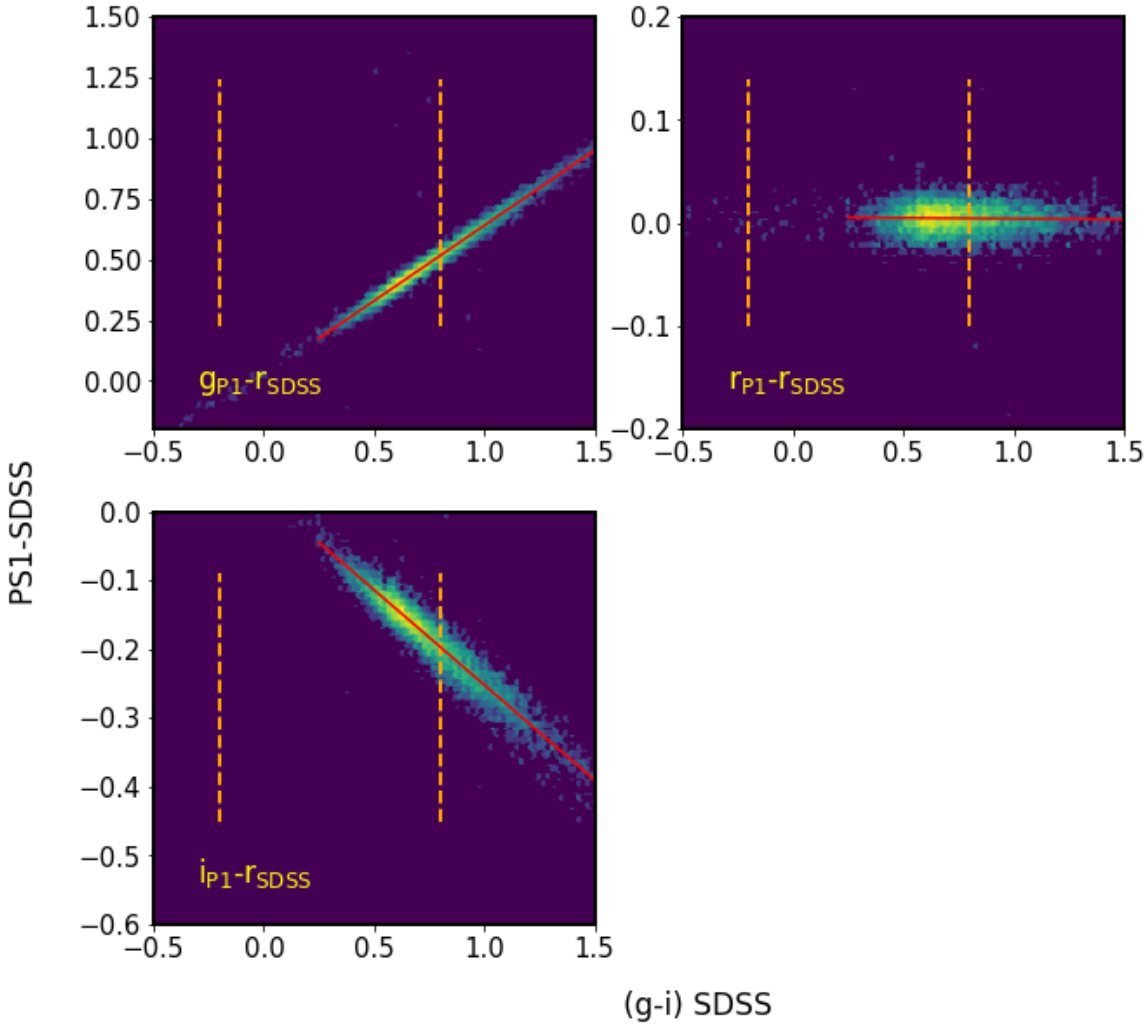

Figure 4. The SDSS-PS1 offsets. We plot only bright stars where SDSS $r < 19$, and that fulfill mErr * sqrt(Nobs) ¡ 0.03 . Each panel includes about 6000 standard stars. Vertical dashed lines mark the region in the SDSS color space occupied by quasars (see Fig. 3), used to fit the stellar locus with a polynomial.

object-by-object M10 to our SDSS-only results we find a very good agreement - histograms on Fig. 11 are peaked around 0.

5.1. *Rest-frame Wavelength Correction*

Prior to looking for correlations with physical quantities (black hole mass, luminosities, redshifts), we correct τ and SF_∞ for wavelength dependence using formulae from M10. Since quasars are at different redshifts, the same observed band would probe a different rest-frame wavelength λ_{RF} for each quasar. We find that the power law employed by M10:

$$f \propto \left(\frac{\lambda_{RF}}{4000\mathring{A}}\right)^B \tag{15}$$

together with the fit coefficients $B = -0.479$ and 0.17 for SF_∞ and τ, respectively, are adequate for our combined SDSS r-band results, as shown on Fig. 12 .

5.2. *Trends with Luminosity, Black Hole Mass, and Redshift*

Here we examine the main scientific results: correlations between variability parameters $(\tau, SF\infty)$, and the physical properties of quasars: absolute i-band magnitude M_i, and black hole mass M_{BH}.

First, we consider the selection effects that are inherent to the quasar distribution. Fig. 13 shows the distribution of quasars as a function of redshift z, i magnitude M_i, and black hole mass M_{BH}. For instance, the trend of increasing redshift with M_i on the upper left panel is due to the fact that quasars have to be brighter to be included in the survey at increasing distances.

As explained in (Shen et al. 2008, 2011), the most common approach to estimate quasar black hole mass is to assume that the broad-line region (BLR) is virialized, so that the continuum luminosity can be used as a proxy

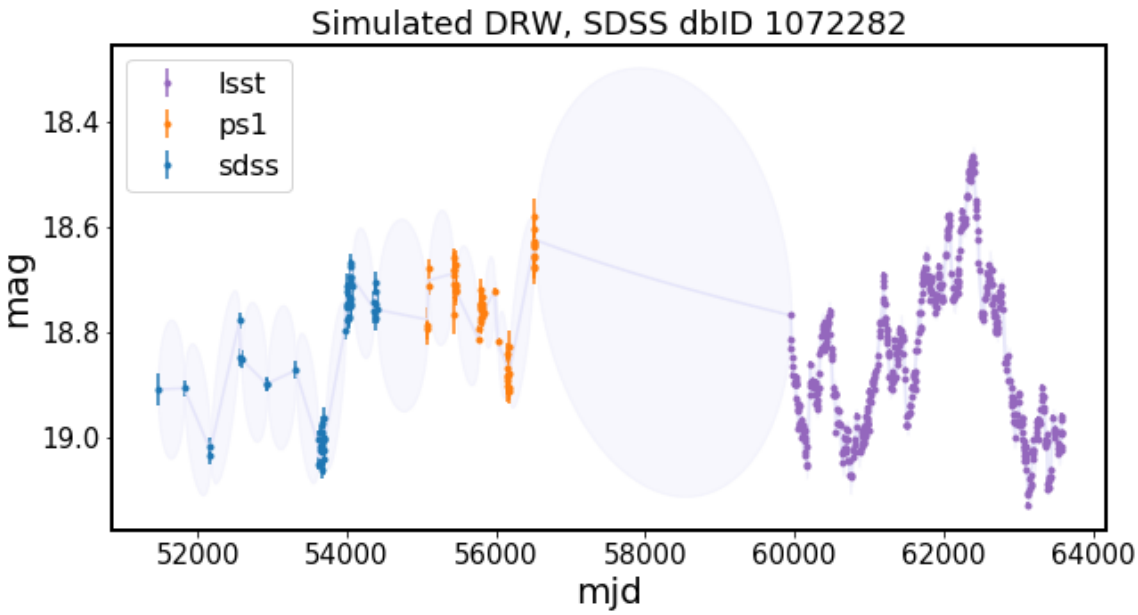

Figure 5. Simulated DRW process sampled at the real cadence of SDSS, PS1 segments for quasar SDSSdbID=1072282, adding the simulated LSST segment. The well-sampled true DRW signal was first sampled at SDSS-PS1-LSST cadences, and then Gaussian offset was added to each point to simulate observational noise.

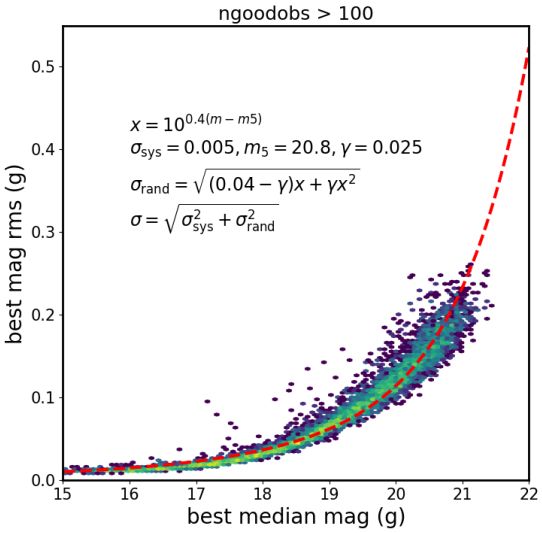

Figure 6. The rms spread as a function of magnitude for ZTF non-variable stars with over 100 observations. We overplot the functional describing the adopted error model (after Ivezić et al. 2019). Properties of ZTF photometric uncertainties are largely similar to the PTF uncertainties.

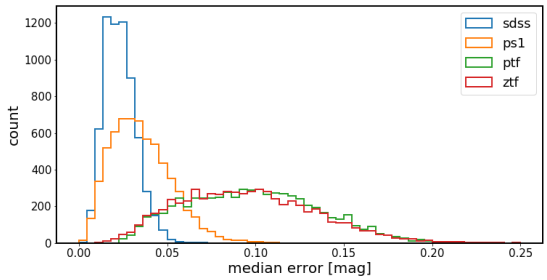

Figure 7. Distribution of median photometric uncertainties (colloquially called 'errors') in combined r-band real light curves. This shows that the PTF and ZTF segments have much larger errors than SDSS, PS1. This is the reason for using only SDSS-PS1 part of the combined light curve.

for the BLR radius, and the width of the broad emission lines (or line dispersion) is used to compute the virial velocity. The most commonly used, calibrated emission lines, that are available across different redshifts, are broad Hα, Hβ, Mg II, and C IV (Vestergaard 2002).

There are various available catalogs of quasar properties : redshift, absolute i-band luminosity, black hole mass. Usually the first quasar catalog releases basic properties such as redshift and photometry (eg. Schneider et al. 2007, 2010, and then more involved studies derive black hole masses and bolometric luminosities (eg. Shen et al. 2008, 2011). This is also the case for more recent work: once (Pâris et al. 2017) released SDSS DR12 Quasar Catalog (DR12Q), (Kozłowski, Szymon 2017) followed by estimating from photometry the monochromatic luminosities, and deriving black hole masses, and (Chen et al. 2018) added a detailed analysis of continuum luminosities in the Hα, Hβ regions for low-redshift quasars. Using the spectra from Chinese LAMOST survey (Dong et al. 2018) also sought to estimate virial black hole masses, and the results while consistent with (Shen et al. 2011), suffered from necessity to peg the non-calibrated spectra to SDSS photometry which was

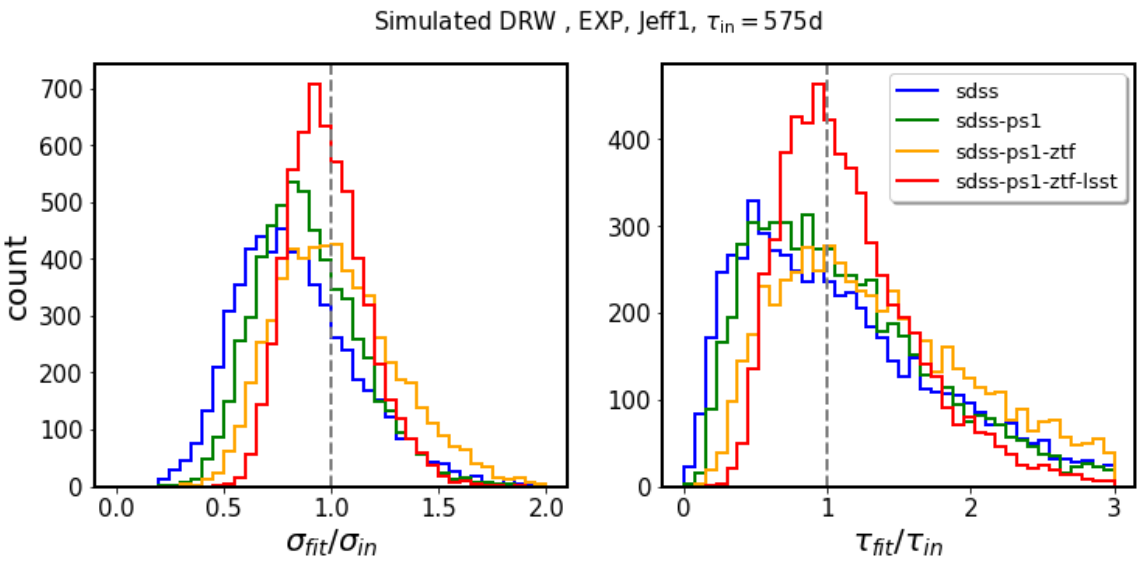

Figure 8. Retrieved τ and σ parameters for simulated LCs.

taken at a different epoch. For sources variable at $\tilde{0}.2$ mag level, such as quasars, the ideal is to use single-epoch calibrated spectra to estimate continuum luminosity, and find virial black hole masses using relationships based on the monochromatic fluxes and broad line widths. Even though Pâris et al. (2018) DR14Q is the most recent catalog, like (Pâris et al. 2017) it lacks black hole masses and bolometric luminosities, and (Kozłowski, Szymon 2017) (henceforth K17) bases his analysis on a SDSS photometry as a proxy for monochromatic luminosities rather than directly from the spectra. Of all available catalogs, (Shen et al. 2011) provides the best to date measurements of quasar black hole masses and monochromatic luminosities, based directly on the single-epoch spectra, and is therefore our choice.

The absolute i-band magnitude M_i is a good proxy for the bolometric luminosity (see Shen et al. 2008, Fig.2). M_i is derived from the observed i-band magnitude, by correcting for Galactic extinction, and K-correcting for the fact that at different redshifts different portions of the spectral energy distribution are observed by the telescope filter bandpass. Historically termed K-correction (Oke & Sandage 1968), $K(z)$ is defined as $m_{intrinsic} = m_{observed} - K(z)$. In the early 2000s the standard was to K-correct to redshift 0, but as (Richards et al. 2006) pointed out, since the distribution of quasars peaks at redshift 2, for most quasars K(z=0) required shifting the observed spectrum into the far infrared. The procedure was to correct separately for the continuum and emission line contributions, assuming a particular spectral shape (eg. power law $f_\nu \propto \nu^\alpha$, with $\alpha = -0.5$ - see Schneider et al. 2010; Vanden Berk et al. 2001; Richards et al. 2006). This introduced large error if the assumed spectral shape $\alpha = -0.5$ was far from the real spectral index. In early 2010s the standard started to shift towards K-correcting to redshift 2 (following Richards et al. 2006; Wisotzki 2000; Blanton et al. 2003), and including custom qusasar spectral shapes, as we see eg. in the catalog of (Shen et al. 2011). Thus in this study we use the absolute i-band magnitude K-corrected to z=2: $M_i(z = 2)$ from (Shen et al. 2011).

We show on Fig. 14 τ and SF_∞ as a function of absolute magnitude M_i, redshift z, and black hole mass M_{BH}. We investigate these correlations in more detail fitting to f is τ_{RF} or SF_∞ a power law :

$$\log_{10} f = A + B \log_{10}\left(\lambda_{RF}/4000\mathring{A}\right) + C(M_i + 23) + D \log_{10}\left(M_{BH}/10^9 M_\odot\right) \quad (16)$$

M10 fitted this power law independently to each of the five SDSS bands, reporting the band-averaged coefficients. Fig. 15 shows the example of posterior samples for $f = SF_\infty$ correlating the M10 SDSS ugriz data against an updated quasar catalog of (Shen et al. 2011).

Because we use the combined r-band data, we compare our results to M10 SDSS r-band only. We have already shown consistency of object-by-object results when using only SDSS segment in Figs. 10 and 11. Now we show that the trends recovered using SDSS-only portions are also consistent with M10. Fig. 17 shows the results for $f = SF_\infty$ - we find that there is a larger dependence of variability amplitude on quasar luminosity, but smaller dependence on black hole mass. Fig. 16 concerns the τ, which appears to be less correlated with both quasar luminosity and black hole mass.

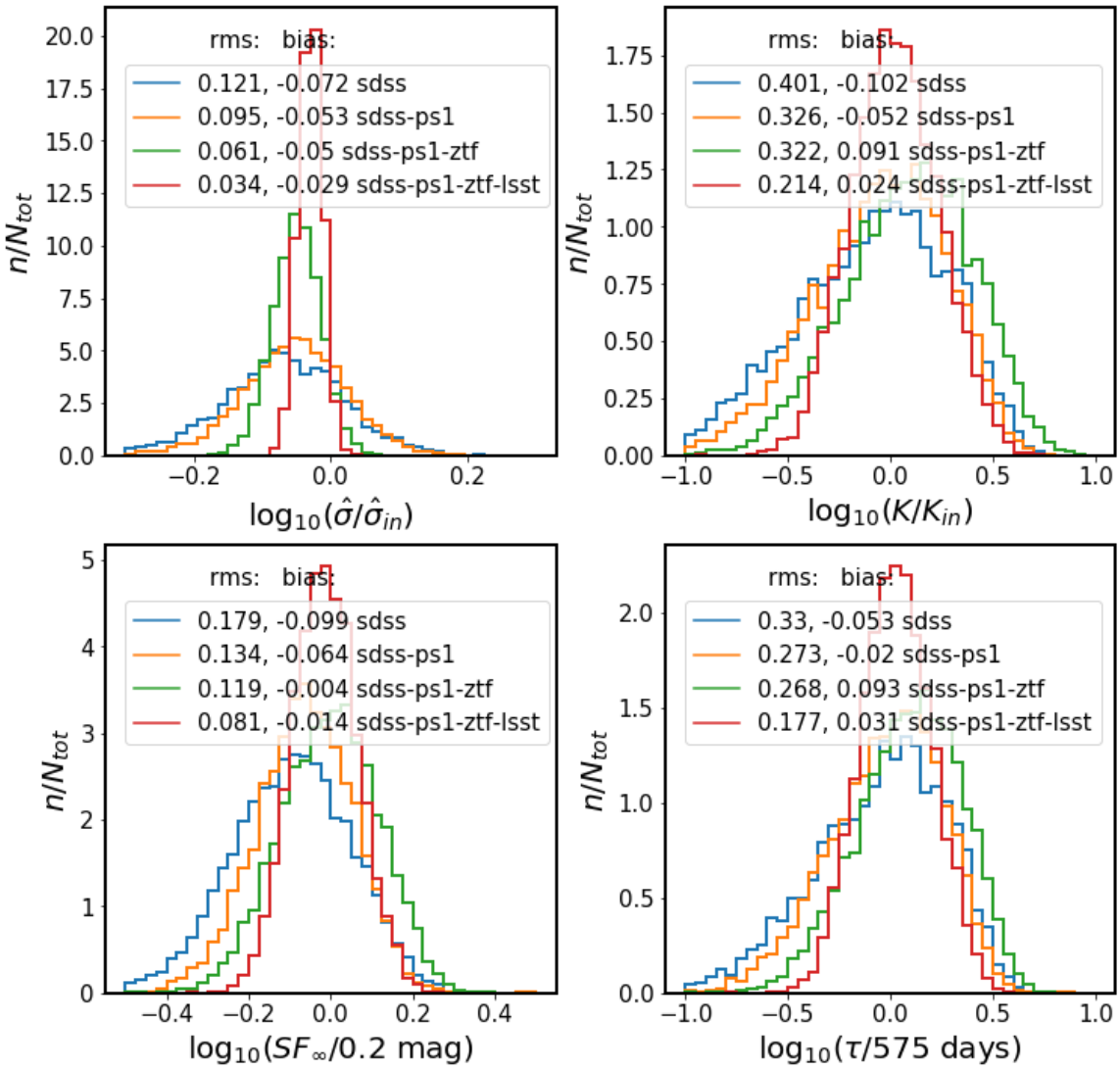

Figure 9. Comparison of retrieved parameters in relation to input parameters, shown as Fig.18 in MacLeod et al. (2011)

5.3. *Comparison with other studies*

Sun et al. (2018) using 1000 low-z S82 QSO finds that variability amplitude is correlated with the inverse of bolometric luminosity, and suggests that since $\hat{\sigma}$ is so well related to L_{bol}, perhaps we could use the $\hat{\sigma} - L_{bol}$ relation to derive L_{bol} without assuming any cosmological models. Our work suggests that with added PS1 data, τ is more strongly dependent on luminosity than with only SDSS data. This is consistent with findings of Sun et al. (2018), who concluded with Structure Function analysis of their luminosity-matched quasar sample, that τ depends mostly on the bolometric luminosity.

In principle any tight correlation between the variability parameters and physical properties of quasars could be used to infer eg. black hole mass or bolometric luminosity given only the optical time-series. In the era of large synoptic surveys (PS1, ZTF,LSST), this could provide additional information about quasars for which it will be impractical to obtain a spectrum (Sánchez-Sáez et al. 2018).

The dominant trend in quasar properties is the Eigenvector-1 : the anti-correlation between the broad line Fe II emission, and the strength of the narrow OIII (5007$\mathring{A}$) lineWang et al. (1996). (Shen & Ho 2014) argued from quasar clustering analysis that the entire diversity of quasars in the quasar main sequence can be explained by variation in accretion (expressed in $R_{\rm FeII}$ - the ratio of the equivalent width of FeII between $4435 - 4685$ $\mathring{A}$ and Hβ), or orientation effects (affecting the full-width at half-maximum of the Hβ broad line). In particular, (Shen & Ho 2014) suggests that $R_{\rm FeII}$ increases with the Eddington ratio, i.e. is anticorrelated with M_{BH}. This finding was confirmed by Sun & Shen (2015) with measurements of black hole mass

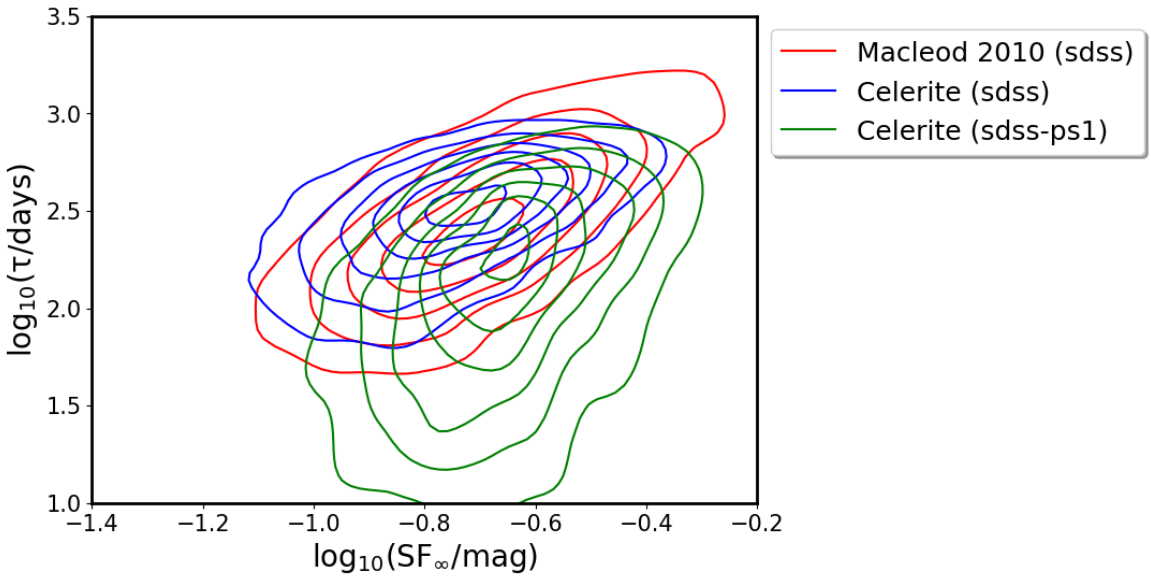

Figure 10. Comparing the rest-frame timescales τ, and asymptotic variability amplitudes SF_∞, for M10 SDSS r-band, and combined SDSS and PS1 data.

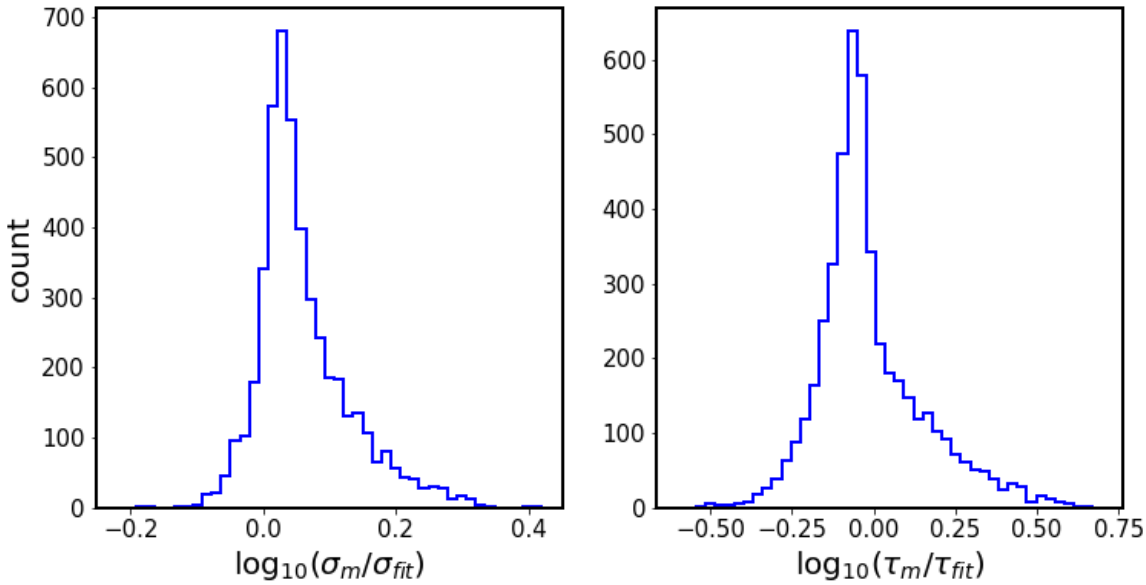

Figure 11. Plot comparing results for SDSS r-band fitting of M10 (σ_m, τ_m), and current results for SDSS r-band using Celerite $(\sigma_{fit}, \tau_{fit})$.

from the quasar host galaxy stellar dispersion σ_* (using the $M_{BH} - \sigma_*$ relation - Ferrarese & Merritt 2000; Kormendy & Ho 2013). For this reason, (Sun et al. 2018) chose to explore the evolution of quasar variability in narrow redshift range, as a function of $R_{\rm FeII}$ and L_{bol}.

X-ray reprocessing is also consistent with the dependence of $\hat{\sigma}$ on the FeII strength, studied by (Sun et al. 2018).

Part of the unaccounted for scatter could be due to variations in metallicity. As Jiang et al. (2016) points out based on three-dimensional radiation magnetohydrodynamic simulations, the iron opacity bump may have a strong influence on the stability of an accretion disk, and thus link metallicity to AGN variability. This would also be consistent with findings of Sun et al. (2018) if quasars with high FeII strength have higher metallicity, and have more stable disks.

(Guo et al. 2017) uses a low-redshift (z¡1.2), low black hole mass ($\log_{10}(M_{BH} < 9)$) subsample of the SDSS

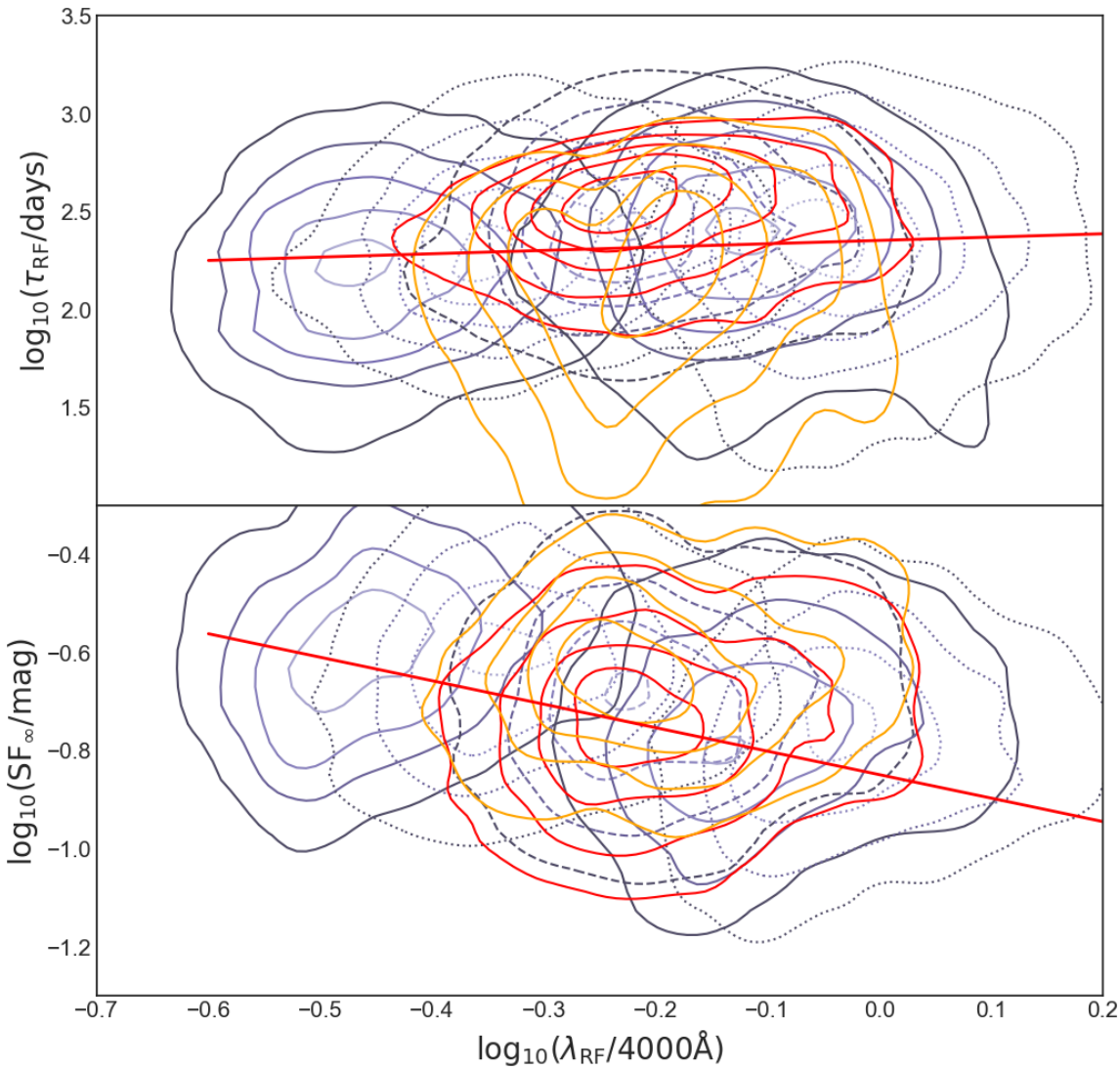

Figure 12. Rest-frame timescale τ (top panel), and asymptotic structure function SF_∞ (bottom panel), as a function of rest-frame wavelength λ_{RF}. The background contours show M10 SDSS *ugriz* data, and the foreground contours denote our results using SDSS (red) and SDSS-PS1 (orange) segments. The red line indicates the best-fit power law to M10 data, with $B = 0.17$ an -0.479 for τ_{RF}, and SF_∞, respectively.

S82 r-band quasar light curves. Using Javelin Zu et al. (2011) code they fitted DRW model for τ, SF_∞

The variability on several years timescale can be explained by the reprocessing model Kokubo (2015), assuming that the AGN UV-optical variability is a results of reprocessing of X-ray or far-UV emission (Krolik et al. 1991)

(Sánchez-Sáez et al. 2018) combined the SDSS spectra with 5 year light curves of 2345 quasars obtained with Quasar Equatorial Survey Team (QUEST)-La Silla AGN Variability Survey. Using the Bayesian parametrization of Structure Function (Schmidt et al. 2010), $\mathrm{SF}(\tau) = A(\tau/1\mathrm{yr})^\gamma$, they found that the amplitude of variability A is anti-correlated with rest-frame emission wavelength, and Eddington ratio (similar as M10). Due to limited light curve length they did not consider any correlations with τ. The decreasing of A with increasing λ_{rest} would naturally follow from the inner regions of the disk being more variable (higher amplitude and shorter wavelength) - see (Fausnaugh et al. 2016) and (Edelson et al. 2015). The anticorrelation of A and Eddington ratio is consistent with other works (M10, Simm et al. 2016, Rakshit & Stalin 2017)

Since multiple studies have found t

5.4. *Alternative method to estimate black hole masses*

In an absence of time-series for a quasar, an attractive alternative method to estimate black hole masses is presented by (Kozłowski 2015). Broad-band AGN pho-

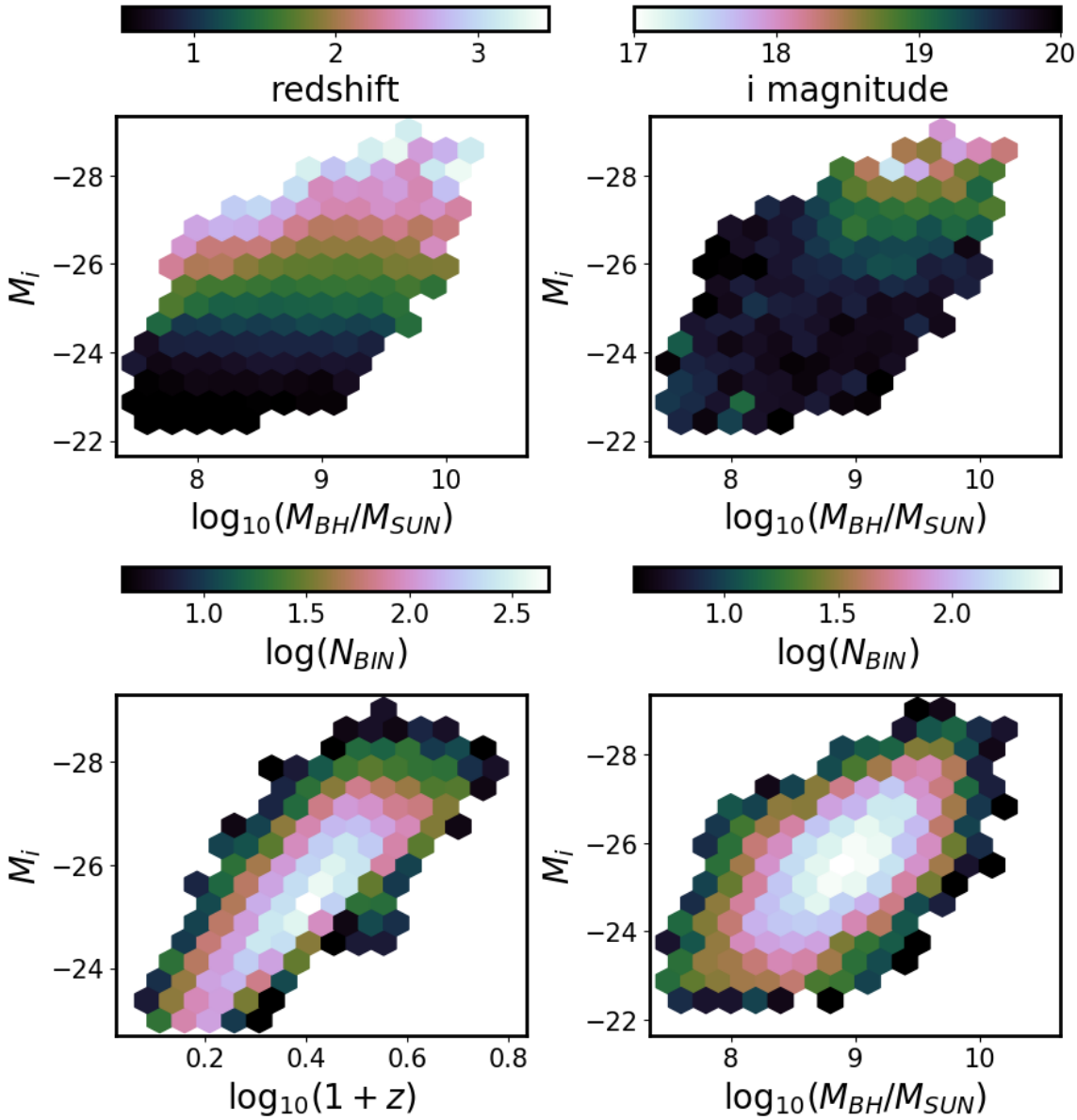

Figure 13. Distribution of quasars as a function of redshift, observed i-band magnitude, absolute i-band magnitude (K-corrected to z=2), and virial black hole mass. All quantities from (Shen et al. 2011).

tometry can be translated into monochromatic fluxes in the vicinity of the reverberating lines (Hβ 5100 $\AA$, Mg II at 3000 $\AA$, and C IV at 1350 $\AA$, Kozłowski 2015), which in turn can be used to estimate the virial black hole mass :

$$M_{BH} = \frac{fR\Delta V^2}{G} \tag{17}$$

where f is a constant of order unity, R is the size of the Broad Line Region (estimated from emission-line lag Δt as $R = c\Delta t$), ΔV is the emission line width, G gravitational constant. From reverberation mapping studies we know that continuum luminosity L is related to the size of the BLR region as $R \propto L^{\gamma}$ (Vestergaard & Peterson 2006), with γ very close to 1/2 (eg. Bentz et al. 2009 finds from RM studies $\gamma = 0.519 \pm 0.06$). Thus we obtain that $R\Delta V^2 \propto L^{\gamma}\Delta V^2 \equiv \mu$, and the black hole mass is a simple function of line width measurement and continuum luminosity :

$$\log M_{BH} = \log \mu + a \tag{18}$$

This is also seen eg. in more recent study by (Shen et al. 2018) of the SDSS Reverberation Mapping sample.

Ideally one would obtain a quasar spectrum to directly measure ΔV and L, and use Eq.18 to estimate the black hole mass. In the era of LSST, with an order of magni-

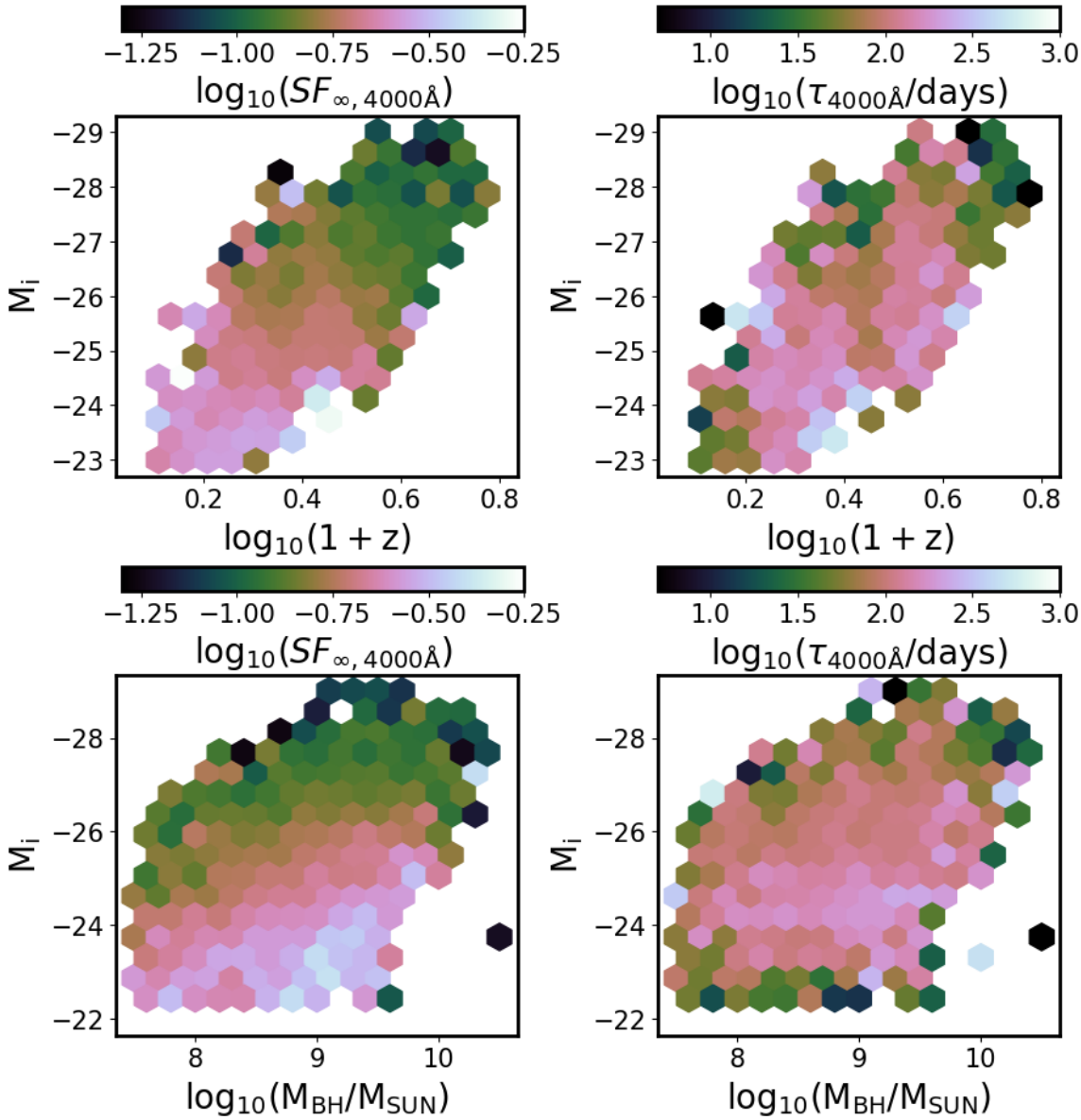

Figure 14. Long-term variability (SF_∞), and characteristic timescale (τ), as a function of absolute i-band magnitude (K-corrected to redshift 2, proxy for bolometric luminosity), virial black hole mass, and redshift.

tude increase in the number of known quasars, spectroscopic follow-up of all is not feasible, but as long as the broad-band photometry is available, (Kozłowski 2015) method (also applied to SDSS Quasar Data Release 12, see Kozłowski 2017) presents an attractive alternative to the variability-based black hole mass estimates.

Anticorrelation of variability amplitude and the Eddington ratio has a variety of possible explanations.

In thin disk theory Shakura & Sunyaev (1973); Frank et al. (2002); Netzer (2013), radius of the emission region at given wavelength increases with the Eddington ratio, and is inversely proportional to temperatureRakshit & Stalin (2017). Thus a hotter disk means that the emission observed in a given bandpass is emitted from a larger radius. From causality, a smaller region can be more variable than a larger one. Therefore, a hotter disk would be less variable at a given wavelength than a colder one, and the variability amplitude as studied in a particular bandpass (here, SDSS r-band) would be anticorrelated with Eddington ratio.

Rakshit & Stalin (2017) notes that as the Eddington ratio increases, the radius of emission at a given wavelength increases (higher L/L_{Edd} - hotter disk), leading to a decreased variability amplitude.

If Eddington ratio is related

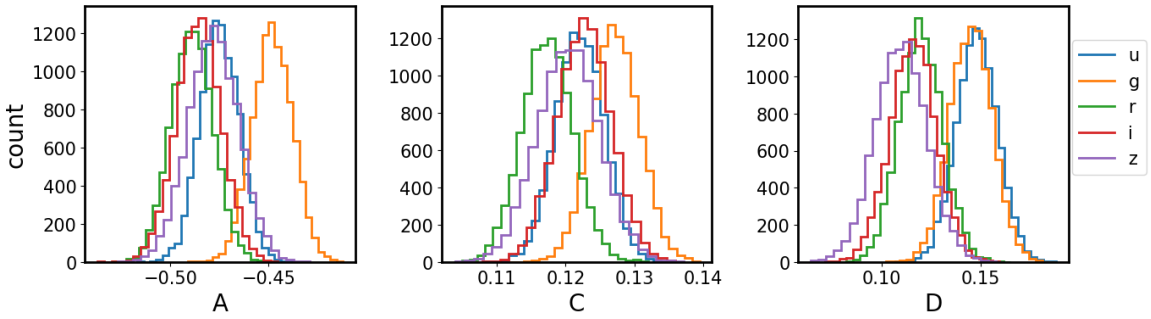

Figure 15. Table 1 in M10 reported the band-averaged values for fit coefficients A,C,D for Eq. 16. Shown here are samples from posterior MCMC draws using M10 results for $f = SF_\infty$, against Shen et al. 2011 M_i and M_{BH}. Because the SDSS r-band results are different from band-averaged values, we compare our SDSS-PS1 combined r-band results against M10 SDSS r-band only.

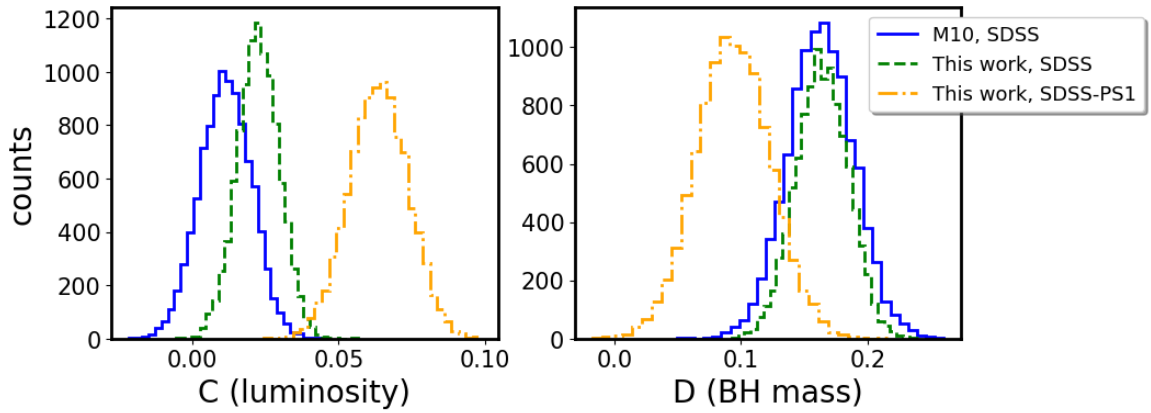

Figure 16. Comparison of our fits to Eq. 16, for $f = \tau$ with SDSS only, or SDSS-PS1 combined quasar light curves, against M10 SDSS r-band. The results from SDSS-only portion are consistent with M10 for the single band. Inclusion of the PS1 portion decreases the timescale dependence on black hole mass, but increases the luminosity dependence. This can be understood as a rotation of the plane in (τ, M_i, M_{BH}) coordinates.

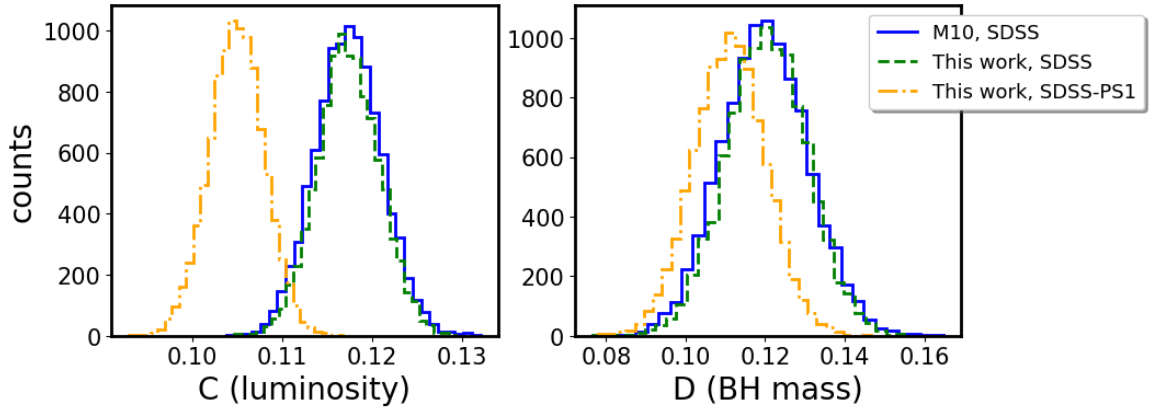

Figure 17. Same as Fig. 16, but fitting quasar absolute magnitude, and black hole mass in Eq. 16 as a function of the asymptotic amplitude $f = SF_\infty$. New data from PS1 supports a weaker dependence of variability amplitude with luminosity and black hole mass.

Table 1. Color terms (offsets) between the following survey filters and SDSS(r) band, using the mean SDSS(g-i) color, so that the synthetic SDSS(r) magnitude can be found as $r_{SDSS,synth} = x - B_0 - B_1 SDSS(g-i)$

Band (x)	B_0	B_1
CRTS V	-0.0464	-0.0128
PTF g	-0.0294	0.6404
PTF R	0.0058	-0.1019
PS1 g	0.0194	0.6207
PS1 r	0.0057	-0.0014
PS1 i	0.0247	-0.2765

NOTE—To derive the offsets we used SDSS S82 1 mln standard stars catalog (Ivezić et al. 2007). We randomly selected 10% of that catalog, for which 48250 have CRTS light curves with at least 10 observations (B.Sesar). For these stars we obtained PS1 photometry from MAST http://panstarrs.stsci.edu and PTF from IRSA PTF Object Catalog https://irsa.ipac.caltech.edu/. We further imposed quality cuts requiring that the stars are bright: $r < 19$.

In the era of changing-look active galaxies (including initially distinct classes of Changing-Look Quasars (LaMassa et al. 2015; MacLeod et al. 2019), Changing-Look AGNs (Marchese et al. 2012; Bianchi et al. 2009; Risaliti et al. 2009), Changing-Look LINERS (Frederick et al. 2019) to name a few) there is a revived interest in possibly linking the behavior of stellar-sized accreting systems (eg. Black Hole Binaries), to that of galactic scale (eg. AGN, QSO, LINERS)(Noda & Done 2018).

It appears that there are several timescales at play, and possibly several interlinked mechanisms that drive the variability.

One possibility

There is a hierarchy of relevant timescales in the standard optically thick, geometrically thin, α-disk model : dynamical, thermal, front, viscous, with $t_{dyn} < t_{th} < t_{front} < t_{visc}$ (Netzer 2013; Frank et al. 2002).

The dynamical, or gas orbital, timescale is simply an inverse of the Keplerian orbital angular frequency Ω at radius R :

$$t_{dyn} \sim 1/\Omega = \left(\frac{GM}{R^3}\right)^{-1/2} \tag{19}$$

The main parameter describing the accretion disk is α - the ratio of the (vertically averaged) total stress to thermal (vertically averaged) pressure (Lasota 2016) :

$$\alpha = \frac{\langle \tau_{r\varphi} \rangle_z}{\langle P \rangle_z} \tag{20}$$

After Lasota (2016), the hydrodynamical stress tensor is:

$$\tau_{r\varphi} = \rho\nu \frac{\partial v_\varphi}{\partial R} = \rho\nu \frac{d\Omega}{d\ln R} = \frac{3\rho\nu\Omega}{2} \tag{21}$$

so with c_s - local sound speed at radius R (isothermal sound speed is $c_s = \sqrt{P/\rho}$),

$$\alpha = \frac{3\rho\nu\Omega}{2P} = \frac{3\Omega\nu}{2c_s^2} \tag{22}$$

This means that less viscous disks have smaller α.

The thermal timescale - for re-adjustment to thermal equilibrium (derived in detail in Frank et al. (2002)), is the ratio of heat content per unit disk area to dissipation rate per unit disk area : $(dE/A)/(dE/dt/A) = dt$. The heat content per unit volume is $\sim \rho kT/\mu m_p \sim \rho c_s^2$, and heat content per unit area is that divided by the scale height $\sim \rho c_s^2/h \sim \Sigma c_s^2$. Meanwhile, the dissipation rate per unit area, $D(R)$, is

$$D(R) = \frac{9}{8}\nu\Sigma R^{-3} GM \tag{23}$$

(eq. 4.30 in Frank et al. 2002), so :

$$t_{th} \sim$$

The cooling and heating fronts propagate through the disk at αc_s (Hameury et al. 2009) - in that description with no viscosity there is no communication between neighboring disk annuli, and thus no front propagation (Balbus & Hawley 1998; Balbus 2003). Following Stern et al. (2018), if we define as h/R the the disk aspect ratio, with the disk height $h = c_s/\Omega$, and , the characteristic time for front propagation is:

$$t_{front} \sim (h/R)^{-1} t_{th} \tag{25}$$

The viscous timescale is the characteristic time it would take for a parcel of material to undergo a radial transport due to the viscous torques from the radius R to the black hole (Czerny 2006). Note that while the

viscosity has probably magnetic origin(Eardley & Lightman 1975; Grzedzielski et al. 2017), we use a hydrodynamical description of accretion flow. With $\nu = \eta/\rho$ (kinematic viscosity being the ratio of dynamical viscosity to density), Frank et al. (2002) shows (Chap.5.2) that

$$t_{visc} \sim R^2/\nu \sim R/v_R = (h/R)^{-2} t_{th} \quad (26)$$

6. CONCLUSIONS

REFERENCES

AlSayyad, Y. 2016, PhD thesis, University of Washington. http://hdl.handle.net/1773/37020

Ambikasaran, S., Foreman-Mackey, D., Greengard, L., Hogg, D. W., & O'Neil, M. 2015, IEEE Transactions on Pattern Analysis and Machine Intelligence, 38, doi: 10.1109/TPAMI.2015.2448083

Annis, J., Soares-Santos, M., Strauss, M. A., et al. 2014, ApJ, 794, 120, doi: 10.1088/0004-637X/794/2/120

Aranzana, E., Körding, E., Uttley, P., Scaringi, S., & Bloemen, S. 2018, MNRAS, 476, 2501, doi: 10.1093/mnras/sty413

Balbus, S. A. 2003, ARA&A, 41, 555, doi: 10.1146/annurev.astro.41.081401.155207

Balbus, S. A., & Hawley, J. F. 1998, Reviews of Modern Physics, 70, 1, doi: 10.1103/RevModPhys.70.1

Bauer, A., Baltay, C., Coppi, P., et al. 2009, ApJ, 696, 1241, doi: 10.1088/0004-637X/696/2/1241

Bentz, M. C., Peterson, B. M., Netzer, H., Pogge, R. W., & Vestergaard, M. 2009, ApJ, 697, 160, doi: 10.1088/0004-637X/697/1/160

Bianchi, S., Piconcelli, E., Chiaberge, M., et al. 2009, ApJ, 695, 781, doi: 10.1088/0004-637X/695/1/781

Blanton, M. R., Lin, H., Lupton, R. H., et al. 2003, AJ, 125, 2276, doi: 10.1086/344761

Borucki, W. J., Koch, D., Basri, G., et al. 2010, Science, 327, 977, doi: 10.1126/science.1185402

Cai, Z.-Y., Wang, J.-X., Gu, W.-M., et al. 2016, ApJ, 826, 7, doi: 10.3847/0004-637X/826/1/7

Caplar, N., Lilly, S. J., & Trakhtenbrot, B. 2017, ApJ, 834, 111, doi: 10.3847/1538-4357/834/2/111

Chambers, K. C. 2011, in Bulletin of the American Astronomical Society, Vol. 43, American Astronomical Society Meeting Abstracts #218, 113.01

Chen, Z.-F., Pan, D.-S., Pang, T.-T., & Huang, Y. 2018, ApJS, 234, 16, doi: 10.3847/1538-4365/aa9d90

Czerny, B. 2006, in Astronomical Society of the Pacific Conference Series, Vol. 360, AGN Variability from X-Rays to Radio Waves, ed. C. M. Gaskell, I. M. McHardy, B. M. Peterson, & S. G. Sergeev, 265

Dexter, J., & Agol, E. 2011, ApJL, 727, L24, doi: 10.1088/2041-8205/727/1/L24

Dexter, J., & Begelman, M. C. 2019, MNRAS, 483, L17, doi: 10.1093/mnrasl/sly213

Dong, X. Y., Wu, X.-B., Ai, Y. L., et al. 2018, AJ, 155, 189, doi: 10.3847/1538-3881/aab5ae

Drake, A. J., Djorgovski, S. G., Mahabal, A., et al. 2009, ApJ, 696, 870, doi: 10.1088/0004-637X/696/1/870

Eardley, D. M., & Lightman, A. P. 1975, ApJ, 200, 187, doi: 10.1086/153777

Edelson, R., Vaughan, S., Malkan, M., et al. 2014, ApJ, 795, 2, doi: 10.1088/0004-637X/795/1/2

Edelson, R., Gelbord, J. M., Horne, K., et al. 2015, ApJ, 806, 129, doi: 10.1088/0004-637X/806/1/129

Edelson, R., Gelbord, J., Cackett, E., et al. 2019, ApJ, 870, 123, doi: 10.3847/1538-4357/aaf3b4

Fausnaugh, M. M., Denney, K. D., Barth, A. J., et al. 2016, ApJ, 821, 56, doi: 10.3847/0004-637X/821/1/56

Ferrarese, L., & Merritt, D. 2000, The Astrophysical Journal, 539, L9, doi: 10.1086/312838

Flewelling, H. 2018, in American Astronomical Society Meeting Abstracts, Vol. 231, American Astronomical Society Meeting Abstracts 231, 436.01

Foreman-Mackey, D., Agol, E., Angus, R., & Ambikasaran, S. 2017, ArXiv e-prints. https://arxiv.org/abs/1703.09710

Foreman-Mackey, D., Bernhard, J., Hoyer, S., Walker, S., & Angus, R. 2018, dfm/george: george v0.3.1, doi: 10.5281/zenodo.1137793. https://doi.org/10.5281/zenodo.1137793

Frank, J., King, A., & Raine, D. J. 2002, Accretion Power in Astrophysics: Third Edition (Cambridge University Press), 398

Frederick, S., Gezari, S., Graham, M. J., et al. 2019, arXiv e-prints, arXiv:1904.10973. https://arxiv.org/abs/1904.10973

Gaskell, C. M., & Peterson, B. M. 1987, ApJS, 65, 1, doi: 10.1086/191216

Graham, M. J., Djorgovski, S. G., Stern, D., et al. 2015, Nature, 518, 74, doi: 10.1038/nature14143

Grzedzielski, M., Janiuk, A., Czerny, B., & Wu, Q. 2017, A&A, 603, A110, doi: 10.1051/0004-6361/201629672

Guo, H., Wang, J., Cai, Z., & Sun, M. 2017, ApJ, 847, 132, doi: 10.3847/1538-4357/aa8d71

Hameury, J.-M., Viallet, M., & Lasota, J.-P. 2009, A&A, 496, 413, doi: 10.1051/0004-6361/200810928

Hernitschek, N., Schlafly, E. F., Sesar, B., et al. 2016, The Astrophysical Journal, 817, 73

Ivezić, Ž., Smith, J. A., Miknaitis, G., et al. 2007, AJ, 134, 973, doi: 10.1086/519976

Ivezić, Ž., Kahn, S. M., Tyson, J. A., et al. 2019, ApJ, 873, 111, doi: 10.3847/1538-4357/ab042c

Jiang, Y.-F., Davis, S. W., & Stone, J. M. 2016, ApJ, 827, 10, doi: 10.3847/0004-637X/827/1/10

Kasliwal, V. P., Vogeley, M. S., & Richards, G. T. 2015, MNRAS, 451, 4328, doi: 10.1093/mnras/stv1230

Kelly, B. C., Bechtold, J., & Siemiginowska, A. 2009, The Astrophysical Journal, 698, 895

Kelly, B. C., Becker, A. C., Sobolewska, M., Siemiginowska, A., & Uttley, P. 2014, ApJ, 788, 33, doi: 10.1088/0004-637X/788/1/33

Kelly, B. C., Treu, T., Malkan, M., Pancoast, A., & Woo, J.-H. 2013, ApJ, 779, 187, doi: 10.1088/0004-637X/779/2/187

Kokubo, M. 2015, MNRAS, 449, 94, doi: 10.1093/mnras/stv241

Kormendy, J., & Ho, L. C. 2013, ARA&A, 51, 511, doi: 10.1146/annurev-astro-082708-101811

Kozłowski, S. 2015, AcA, 65, 251. https://arxiv.org/abs/1504.05960

Kozłowski, S. 2016, MNRAS, 459, 2787, doi: 10.1093/mnras/stw819

Kozłowski, S. 2017, ApJS, 228, 9, doi: 10.3847/1538-4365/228/1/9

Kozłowski, S., Kochanek, C. S., Udalski, A., et al. 2010, ApJ, 708, 927

Kozłowski, Szymon. 2017, A&A, 597, A128, doi: 10.1051/0004-6361/201629890

Krolik, J. H., Horne, K., Kallman, T. R., et al. 1991, ApJ, 371, 541, doi: 10.1086/169918

Kubota, A., & Done, C. 2018, MNRAS, 480, 1247, doi: 10.1093/mnras/sty1890

LaMassa, S. M., Cales, S., Moran, E. C., et al. 2015, ApJ, 800, 144, doi: 10.1088/0004-637X/800/2/144

Lasota, J.-P. 2016, in Astrophysics and Space Science Library, Vol. 440, Astrophysics of Black Holes: From Fundamental Aspects to Latest Developments, ed. C. Bambi, 1

Li, Z., McGreer, I. D., Wu, X.-B., Fan, X., & Yang, Q. 2018, ApJ, 861, 6, doi: 10.3847/1538-4357/aac6ce

MacLeod, C. L., Ivezić, Ž., Kochanek, C. S., et al. 2010, The Astrophysical Journal, 721, 1014

MacLeod, C. L., Brooks, K., Ivezić, Ž., et al. 2011, The Astrophysical Journal, 728, 26

MacLeod, C. L., Ivezić, Ž., Sesar, B., et al. 2012, The Astrophysical Journal, 753, 106

MacLeod, C. L., Green, P. J., Anderson, S. F., et al. 2019, ApJ, 874, 8, doi: 10.3847/1538-4357/ab05e2

Marchese, E., Braito, V., Della Ceca, R., Caccianiga, A., & Severgnini, P. 2012, Monthly Notices of the Royal Astronomical Society, 421, 1803, doi: 10.1111/j.1365-2966.2012.20445.x

McGreer, I. D., Fan, X., Jiang, L., & Cai, Z. 2018, AJ, 155, 131, doi: 10.3847/1538-3881/aaaab4

McGreer, I. D., Jiang, L., Fan, X., et al. 2013, ApJ, 768, 105, doi: 10.1088/0004-637X/768/2/105

Mushotzky, R. F., Edelson, R., Baumgartner, W., & Gandhi, P. 2011, The Astrophysical Journal, 743, L12, doi: 10.1088/2041-8205/743/1/l12

Netzer, H. 2013, The Physics and Evolution of Active Galactic Nuclei (Cambridge University Press)

Noda, H., & Done, C. 2018, MNRAS, 480, 3898, doi: 10.1093/mnras/sty2032

Oke, J. B., & Sandage, A. 1968, ApJ, 154, 21, doi: 10.1086/149737

Palanque-Delabrouille, N., Magneville, C., Yèche, C., et al. 2013, A&A, 551, A29, doi: 10.1051/0004-6361/201220379

Pâris, I., Petitjean, P., Ross, N. P., et al. 2017, A&A, 597, A79, doi: 10.1051/0004-6361/201527999

Pâris, I., Petitjean, P., Aubourg, É., et al. 2018, A&A, 613, A51, doi: 10.1051/0004-6361/201732445

Peterson, B. M., Ferrarese, L., Gilbert, K. M., et al. 2004, ApJ, 613, 682, doi: 10.1086/423269

Rakshit, S., & Stalin, C. S. 2017, ApJ, 842, 96, doi: 10.3847/1538-4357/aa72f4

Rau, A., Kulkarni, S. R., Law, N. M., et al. 2009, PASP, 121, 1334, doi: 10.1086/605911

Richards, G. T., Strauss, M. A., Fan, X., et al. 2006, AJ, 131, 2766, doi: 10.1086/503559

Risaliti, G., Miniutti, G., Elvis, M., et al. 2009, The Astrophysical Journal, 696, 160, doi: 10.1088/0004-637x/696/1/160

Ross, N. P., McGreer, I. D., White, M., et al. 2013, ApJ, 773, doi: 10.1088/0004-637X/773/1/14

Rybicki, G. B., & Press, W. H. 1992, ApJ, 398, 169, doi: 10.1086/171845

Sánchez-Sáez, P., Lira, P., Mejía-Restrepo, J., et al. 2018, ApJ, 864, 87, doi: 10.3847/1538-4357/aad7f9

Schmidt, K. B., Marshall, P. J., Rix, H.-W., et al. 2010, ApJ, 714, 1194, doi: 10.1088/0004-637X/714/2/1194

Schneider, D. P., Hall, P. B., Richards, G. T., et al. 2007, AJ, 134, 102, doi: 10.1086/518474

—. 2008, VizieR Online Data Catalog, 7252
Schneider, D. P., Richards, G. T., Hall, P. B., et al. 2010, AJ, 139, 2360, doi: 10.1088/0004-6256/139/6/2360
Sesar, B., Ivezić, Ž., Lupton, R. H., et al. 2007, AJ, 134, 2236
Shakura, N. I., & Sunyaev, R. A. 1973, A&A, 24, 337
Shen, Y., Greene, J. E., Strauss, M. A., Richards, G. T., & Schneider, D. P. 2008, ApJ, 680, 169, doi: 10.1086/587475
Shen, Y., & Ho, L. C. 2014, Nature, 513, 210, doi: 10.1038/nature13712
Shen, Y., Richards, G. T., Strauss, M. A., et al. 2011, ApJS, 194, 45, doi: 10.1088/0067-0049/194/2/45
Shen, Y., Hall, P. B., Horne, K., et al. 2018, arXiv e-prints, arXiv:1810.01447. https://arxiv.org/abs/1810.01447
Simm, T., Salvato, M., Saglia, R., et al. 2016, A&A, 585, A129, doi: 10.1051/0004-6361/201527353
Smith, K. L., Mushotzky, R. F., Boyd, P. T., et al. 2018, ApJ, 857, 141, doi: 10.3847/1538-4357/aab88d
Stern, D., McKernan, B., Graham, M. J., et al. 2018, ApJ, 864, 27, doi: 10.3847/1538-4357/aac726
Sun, J., & Shen, Y. 2015, ApJL, 804, L15, doi: 10.1088/2041-8205/804/1/L15
Sun, M., Xue, Y., Wang, J., Cai, Z., & Guo, H. 2018, ApJ, 866, 74, doi: 10.3847/1538-4357/aae208
Tonry, J. L., Stubbs, C. W., Lykke, K. R., et al. 2012, ApJ, 750, 99, doi: 10.1088/0004-637X/750/2/99
Vanden Berk, D. E., Richards, G. T., Bauer, A., et al. 2001, AJ, 122, 549, doi: 10.1086/321167
Vestergaard, M. 2002, ApJ, 571, 733, doi: 10.1086/340045
Vestergaard, M., & Peterson, B. M. 2006, ApJ, 641, 689, doi: 10.1086/500572
Wang, T., Brinkmann, W., & Bergeron, J. 1996, A&A, 309, 81
Wisotzki, L. 2000, A&A, 353, 861
Yang, J., Fan, X., Wu, X.-B., et al. 2017, AJ, 153, 184, doi: 10.3847/1538-3881/aa6577
Zu, Y., Kochanek, C. S., Kozłowski, S., & Udalski, A. 2013, ApJ, 765, 106, doi: 10.1088/0004-637X/765/2/106
Zu, Y., Kochanek, C. S., & Peterson, B. M. 2011, ApJ, 735, 80